

NANOPARTICLES

https://doi.org/10.1070/QEL16380

Silicon nanoparticles as contrast agents in the methods of optical biomedical diagnostics*

S.V. Zabotnov, F.V. Kashaev, D.V. Shuleiko, M.B. Gongalsky, L.A. Golovan, P.K. Kashkarov, D.A. Loginova, P.D. Agrba, E.A. Sergeeva, M.Yu. Kirillin

Abstract. **The efficiency of light scattering by nanoparticles formed using the method of picosecond laser ablation of silicon in water and by nanoparticles of mechanically grinded mesoporous silicon is compared. The ensembles of particles of both types possess the scattering coefficients sufficient to use them as contrast agents in optical coherence tomography (OCT), particularly in the range of wavelengths 700–1000 nm, where the absorption of both silicon and most biological and mimicking tissues is small. According to the Mie theory the main contribution to the scattering in this case is made by the particles having a relatively large size (150–300 nm). In the experiments on visualising the agar phantom surface by means of OCT, the contrast of the medium boundary, provided by nanoparticles amounted to 14 dB and 30 dB for the ablated particles and the porous silicon powder, respectively. The numerical simulation of OCT images of skin in the presence of nanoparticles, confirmed the efficiency of using them as a contrast agent.**

Keywords: *silicon nanoparticles, pulsed laser ablation, mesoscopic media, spectrophotometry, optical coherence tomography, Monte Carlo method.*

1. Introduction

The possibilities of wide-range changes in physical and optical properties of silicon using the methods of modern nanotechnologies offer promising potentialities of this material not only in electronics for designing new types of transistors [1, 2], sensors [3–5], light-emitting [6] and solar [7, 8] elements, but also in biomedical applications. The latter include the improvement of the efficiency of diagnostics [9–12] and treatment [13–18] of various diseases.

The reasons for using silicon nanoparticles in medical applications are the minimal or zero toxicity confirmed by numerous *in vitro* and *in vivo* experiments [19–21] and the ability of their biodegradation under certain conditions during a few hours [9, 22] (as a rule, via the transformation into the orthosilicic acid [23]). Although, undoubtedly, the issue of biocompatibility of silicon nanoparticles in general and in each particular case should be considered in a complex way, taking into account the size, concentration, chemical purity and stability of the used particles.

To date, a considerable success in the field of the silicon nanoparticle formation for biomedical applications have been achieved using the method of electrochemical etching that makes it possible to obtain porous silicon (PS) consisting of nanocrystals of this material and air pores and possessing high-efficiency photoluminescence (PL). Such structures can be used as PL markers, including application in living organisms [9, 10]. It seems promising to use PS in the treatment of oncologic diseases by means of the photodynamic therapy method due to the possibility of photosensitised generation of singlet oxygen in the ensembles of silicon nanocrystals [13, 14]. The implementation of this idea was experimentally demonstrated in Refs [15, 16] by the example of cancer cells of murine fibroblasts and human lung.

Despite relative cheapness and technological advantages of nanocrystalline silicon using electrochemical etching with possible further grinding into a powder for practical use [9, 10, 15, 16], there are other methods of nanoparticle production, promising for biomedical application. In particular, the laser ablation method is used rather frequently, in which nanoparticles are formed by agglomeration of the products of ablation of the irradiated target in a buffer liquid or gas. The choice of the latter allows the control of not only the size of the produced nanoparticles, but also of their structure, chemical purity and stability, which offers promising potentialities for using such objects in biomedicine. This trend in nanotechnology was called "green synthesis" [24]. To date, laser ablation made it possible to synthesise functional gold nanoparticles, possessing a high degree of biocompatibility with cell cultures [25] and being promising agents not only for the cancer diagnostics, but also for the cancer treatment. Considerable success was achieved in the synthesis of nanoparticles based on the iron oxide [26], which is interesting for diagnostics and laser therapy of degenerative diseases of cartilages [27, 28].

*Presented at the Fundamentals of Laser Assisted Micro- and Nanotechnologies (FLAMN-16) International Symposium (Pushkin, Leningrad oblast, 27 June to 1 July 2016).

S.V. Zabotnov, P.K. Kashkarov Faculty of Physics, M.V. Lomonosov Moscow State University, Vorob'evy Gory, 119991 Moscow, Russia; National Research Centre 'Kurchatov Institute', pl. Akad. Kurchatova 1, 123182 Moscow, Russia; Department of Nano-, Bio-, Information Technology and Cognitive Science, Moscow Institute of Physics and Technology, ul. Maksimova 4, 123098 Moscow, Russia; e-mail: zabotnov@physics.msu.ru;
F.V. Kashaev, D.V. Shuleiko, M.B. Gongalsky, L.A. Golovan Faculty of Physics, M.V. Lomonosov Moscow State University, Vorob'evy Gory, 119991 Moscow, Russia;
D.A. Loginova, P.D. Agrba Lobachevsky State University of Nizhny Novgorod, prosp. Gagarina 23, 603950 Nizhnii Novgorod, Russia;
E.A. Sergeeva, M.Yu. Kirillin Institute of Applied Physics, Russian Academy of Sciences, ul. Ul'yanova 46, 603950 Nizhnii Novgorod, Russia

Received 24 March 2017; revision received 6 May 2017
Kvantovaya Elektronika **47** (7) 638–646 (2017)
Translated by V.L. Derbov

The method of pulsed laser ablation has also proved itself efficient in the formation of silicon nanoparticles. The low-toxic silicon nanocrystals produced in this way appeared suitable both for bioimaging of living organisms [11, 12] and for photosensitised generation of singlet oxygen [17]. It is important to emphasise one more advantage of the pulsed laser ablation method: in most cases, the PL peaks of nanostructured silicon are located in the so-called transparency window of biotissues, i.e., in the spectral range from 700 to 1300 nm [11, 12, 17, 29, 30].

A considerable number of papers devoted to the use of silicon nanoparticles, formed by means of electrochemical etching or laser ablation are related to their application as PL markers. Particular attention in such studies is paid to the PL properties of silicon nanocrystals having a size smaller than 8 nm, which can be also formed using the methods of chemical synthesis in solutions [31, 32], can be biocompatible and, in particular, possess spherical shape and narrow size distribution.

We should note that silicon has a relatively high refractive index (about 3.6 in the red and near-IR spectral regions [33]). Nanoparticles of this material possess a sufficiently large scattering cross section and, therefore, seem to be promising as contrast agents in biotissue visualisation using the methods of optical imaging. Previously, the possibility of controlling the optical properties of biotissues and the contrast in optical imaging methods was demonstrated using nanoparticles of gold [34, 35], titanium dioxide [36], zinc dioxide [37] and other materials [35]. However, practically no studies of the efficiency of silicon nanoparticles used for these applications have been carried out until now.

In our previous paper [38] we have shown the possibility of using silicon nanoparticles, formed by picosecond laser ablation as contrast agents for the visualisation of the surface of agar gel by means of optical coherence tomography (OCT). The essence of this technique of visualising the inner structure of optically inhomogeneous objects with the spatial resolution up to a few micrometres consists in the detection of the probe radiation backscattered by the object of study using the low-coherence interferometry [39].

In the present paper, we consider two types of silicon nanoparticles formed using laser ablation and obtained by mechanical grinding of PS into a powder. These nanosystems *a priori* possess a wide size distribution, which allows not only the integral comparison of their physical and optical characteristics, as well as the efficiency of their use in bioimaging problems, but also the estimation of the contribution of particles having different size to the light scattering.

2. Objects and methods of study

Suspensions of silicon nanoparticles were prepared using the method of pulsed laser ablation of monocrystalline silicon in water. As initial plates for irradiation, we used the moderately doped silicon Si of p^+ type with the crystallographic orientation of the surface (100) and the specific resistance of 10–20 mOhm cm. The irradiation of the target was performed in a cell with distilled water using an EKSPLA PL 2143A picosecond Nd:YAG laser during 30 min with a pulse repetition rate of 10 Hz. The duration and the wavelength of the pulses were 34 ps and 1064 nm, respectively. In more detail, the experiment is described in Refs [38, 40].

The layers of PS were produced using the method of electrochemical etching of monocrystalline Si plates with the same parameters as indicated above. For the etching, we used the solution of 47.5% hydrofluoric acid with ethanol in the 1:1 proportion. Before etching, the substrates of monocrystalline silicon were placed in pure hydrofluoric acid for a few seconds in order to remove the natural oxide film from the surface. In the process of etching, the electric current density varied from 50 to 100 mA cm^{-2}, and the time of etching varied from 15 to 30 min, depending on the etching rate at the given current. The reason was that, on the one hand, it was necessary to maximise the PS layer thickness (since the experiment required a large amount of material to study). On the other hand, the minimal variance of the size of silicon nanocrystals and air pores was needed, which was achieved at a mean layer thickness of about 75 μm. The PS layer thickness was monitored by means of an Olympus BX41optical microscope. The separation of the PS film from the substrate was implemented at the final stage of the electrochemical etching by an abrupt increase in the current density to 700 mA cm^{-2} during a few seconds. In the experiments on measuring the optical constants and the contrast properties, we used the powders of PS, mechanically grinded using a Fritisch PULVERISETTE 7 planetary-type mill and diluted in distilled water. The use of water as the same base for the solutions of silicon particles, obtained by means of pulsed laser ablation and electrochemical etching, allows one to perform the maximally correct comparison of the contrast properties for the silicon, nanostructured using the above methods, keeping in mind the compatibility of water with living organisms for further practical application.

The structure of the silicon nanoparticles formed by laser ablation was studied with a JEOL JEM-1011 transmission electron microscope (TEM), and that of porous silicon and its powders – with a Carl Zeiss Supra 40 scanning electron microscope (SEM). The results obtained for both types of nanoparticles were compared with the data of dynamical light scattering (DLS) study using a Malvern Zetasizer Nano ZS analyser.

The reflection, collimated and total transmission spectra of the suspensions of silicon nanoparticles, placed in a silica cuvette with the separation of 10 mm between the walls, were measured in the range of wavelengths 400–1100 nm using an Analytik Jena SPECORD 250 spectrophotometer equipped with an integrating sphere.

The experiments on OCT visualisation of turbid media with the above ensembles of silicon nanoparticles serving as contrast agents were carried out using an OKT-1300U OCT system (the centre probe radiation wavelength 910 nm). The 0.3% agar gel, on the surface of which the drops of suspensions with silicon nanoparticles were applied, played the role of a biotissue phantom.

The numerical simulation of the OCT images was performed using the algorithm based on the Monte Carlo method [41]. The optical characteristics of the silicon nanoparticles of different size, used in the simulation, were calculated according to the Mie theory [42].

3. Results and discussion

3.1. Structural and optical properties of silicon nanosystems

The analysis of TEM images of silicon nanoparticles obtained using the method of picosecond laser ablation in water revealed the presence of two fractions, possessing high crys-

tallicity degree [29, 40], in accordance with our earlier studies. The first fraction consists of the particles having relatively small size from 2 to 40 nm (Fig. 1a), and the second one contains large clusters having size from 70 to 200 nm (Fig. 1b). The first type of nanoparticles is most probably formed according to the classical mechanism, in which the collisions with the molecules of a buffer medium (in the considered case water) result in the deceleration and agglomeration of silicon ablation products into nanoparticles [43]. The second type of particles, in our opinion, is a product of either coalescence of the first-type particles under sufficiently high temperatures, caused by the irradiation with laser pulses, or the difference in the velocities of the ablation products according to the theory [44] and our previous studies of the picosecond laser ablation dynamics in silicon [45]. The explanation is as follows. The ablation of the target results in the appearance of two components of ablation products, the 'fast' one and the 'slow' one. The first of them consists of faster ablated atoms that experience practically no collisions in the process of expansion. Therefore, the efficiency of agglomeration into nanoparticles in this case is small, giving rise to the formation of a small-size fraction. For the low-velocity component the number of collisions with the molecules of the buffer medium is essentially greater, which, in turn, increases the efficiency of agglomeration into nanoparticles of larger size.

The presence of the fraction of large nanoparticles in a small concentration is also confirmed by the data of DLS, namely, in the size distribution of the particles, presented in Fig. 1c, one can observe a characteristic fracture of the curve at 100 nm. The dashed line in Fig. 1c is drawn to separate the fractions of small and large particles. We should note that the presented distribution integrally reflects only the presence of particles having the size 30–200 nm. The absence of nanoparticles smaller than 30 nm in the TEM observations is explained by the small efficiency of light scattering by these particles in the DLS method and by the overestimation of the hydrodynamic radius in this distribution as compared to the real one. The latter is due to the moderate stability of the studied suspension, characterised by the measured value of electrokinetic potential -31.4 ± 0.9 mV and the possibility of such a close approach of nanoparticles (Fig. 1a) that in the process of scattering they most probably are detected as a single agglomerate. Nevertheless, with the above considerations taken into account, the DLS data are in good qualitative agreement with the TEM data.

The PS films, formed using the method of electrochemical etching under the conditions described above, possess the characteristic pore size from 10 to 70 nm (Fig. 1d). According to the classification of the International Union of Pure and Applied Chemistry (IUPAC) such structures can be classified as mesoporous ones [46]. From the optical point of view such media should be also treated as mesoscopic ones for the visible and near-IR spectral ranges, since for the radiation having these wavelengths the PS, as well as the powders made of it, can be considered neither as homogeneous objects, nor as those having an atomic-scale size. In other words, such media should be considered as randomly inhomogeneous ones. A similar statement is valid for the nanoparticles produced by the laser ablation method.

For practical use in contrasting the biotissue phantom, the PS films were grinded using the planetary-type mill into a powder, the SEM image of which is presented in Fig. 1e. The

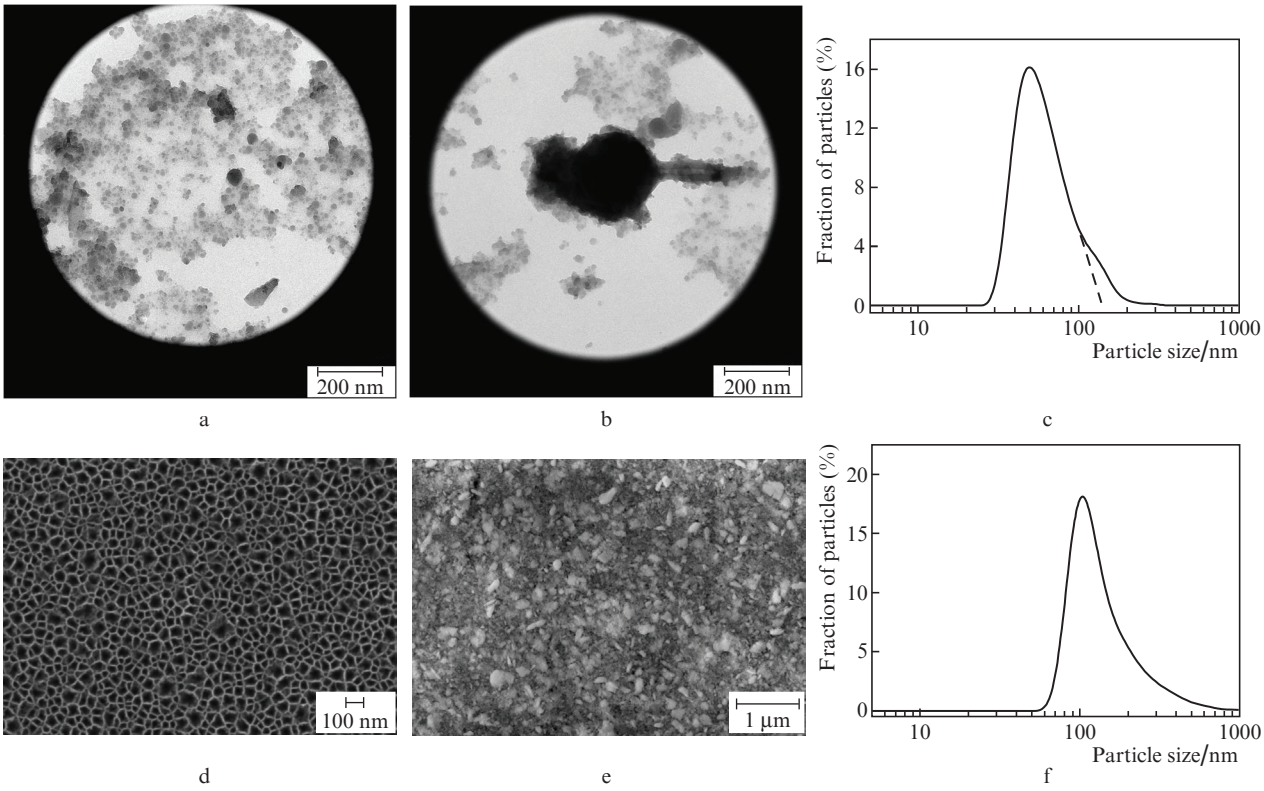

Figure 1. (a, b) TEM images and (c) size distribution of silicon nanoparticles formed by picosecond laser ablation in water. The dashed line in Fig. 1c is drawn to select visually the contribution of the fraction of large particles to the distribution. SEM images of the surface of (d) the initial PS film and (e) the one grinded by means of the planetary-type mill, as well as (f) the size distribution of particles in the resulting PS powder.

powder consisted mainly of the clusters having a size from 50 to 300 nm, which, in turn, were formed by silicon nanocrystallites that were the PS base before grinding. The powder prepared in this way was diluted in water for further study using the methods of spectrophotometry and OCT.

The analysis of the DLS data for the water suspension prepared in this way demonstrates good agreement with the results of SEM. The fraction of nanoparticles having the size 50–300 nm in the distribution presented in Fig. 1f amounts to 81%. The appearance of other particles having the size greater than 300 nm, reflected in the distribution, can be a result of the hydrodynamic radius overestimation in the studied aqueous suspension of silicon nanoparticles, similar to that in the case of nanoparticles ablated in water. Otherwise, they can be real nanoparticles, present in the PS powder in the concentration not exceeding a few percent because of the grinding inhomogeneity.

As seen from Fig. 1, the silicon nanoparticles formed using the methods of laser ablation and electrochemical etching followed by grinding, are ensembles with a nonuniform size distribution, essentially different for each method of preparation. Correspondingly, the optical properties of such nanosystems will differ even in the case of equal concentrations because of the dependence of the light scattering efficiency on the size of the particles that follows from the Mie theory [47]. Therefore, for the comparison of the specific features of scattering and absorption of light by nanoparticles in aqueous suspensions, their concentrations were chosen such that the scattering (μ_s) and absorption (μ_a) coefficients of light would be comparable for each type of nanoparticles, and by the order of magnitude comparable with 0.1 mm^{-1} (Fig. 2). Here, according to the data of weighting the dried suspensions of silicon nanoparticles, their mass concentration amounted to 0.17 g L^{-1} for the laser ablation and to 4.0 g L^{-1} for the grinded PS. With the size distribution of these types of nanoparticles taken into account, the total volume concentrations for each type were estimated as 1.0×10^{13} and 0.34×10^{13} cm^{-3}, respectively.

The optical characteristics of the studied suspensions were determined in the spectral interval 400–1000 nm using the original analytical model of low-multiplicity backscattering. This technique allows the reconstruction of the coefficients μ_s and μ_a from the measured spectrophotometry data, i. e., the spectra of collimated and diffuse transmission and diffuse reflection [38, 48]. The reconstructed dependences of these coefficients are presented in Fig. 2.

A monotonic decrease in the absorption coefficient μ_a with increasing wavelength in Fig. 2 for both types of the studied nanosystems is due to the reduction of light absorption by silicon in the red and near-IR spectral regions [31]. However, we should note that in both considered cases the absorption coefficient asymptotically tends to 0.05 mm^{-1} rather than to zero, as it would be in this spectral region in the case of silicon. The observed effect is most probably caused by the contribution of water to the absorption.

The scattering coefficient μ_s of the suspension of ablated silicon nanoparticles demonstrates an insignificant variation in the range 400–600 nm and a monotonic fall in the range of wavelengths above 600 nm (Fig. 2a), while for the grinded PS powder in water μ_s remains virtually unchanged (Fig. 2b). This behaviour can be explained by the difference in the size of nanoparticles. The relatively large size (50–300 nm) of the PS grinded powder nanoparticles (Fig. 1e) results mainly in

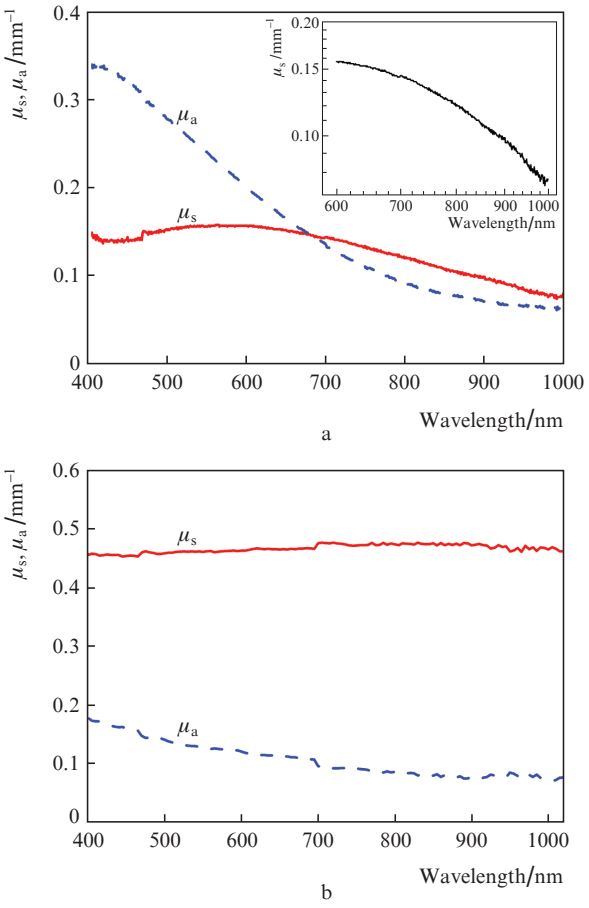

Figure 2. Scattering (μ_s) and absorption (μ_a) coefficients of the silicon nanoparticles prepared using (a) laser ablation and (b) porous silicon powder in water. The inset in Fig. 2a shows the dependence of the scattering coefficient on the wavelength in the logarithmic scale for the spectral range 600–1000 nm.

the Mie scattering in the chosen spectral range. This type of scattering is characterised by a weak wavelength dependence [47], which is confirmed by Fig. 2b.

In the suspension of ablated particles the fraction of those having a size of 2–40 nm is present (Fig. 1a) that gives rise to the Rayleigh scattering. According to the Rayleigh theory, the appropriate contribution decreases as λ^{-4}, where λ is the wavelength of light. The applicability criterion for this theory is that the size of the particle should not exceed $\sim\lambda/15$. Indeed, in the considered case the decrease in μ_s with increasing λ manifests itself above 600 nm, which corresponds to a nanoparticle size of 40 nm, according to the above criterion. In other words, when the wavelength becomes sufficiently large for some of the fractions of the considered nanoparticles (in our case, smaller than 40 nm), then in the experiment it appears possible to detect the contribution of the Rayleigh scattering. It is important to note that the presence of the fraction of larger (70–200 nm) nanoparticles (Fig. 1b) even in small concentrations also contributes to the light scattering, as will be shown below (see Fig. 5b).

However, this type of scattering should be described in terms of the Mie theory. Therefore, the dependence in Fig. 2a is a sum of the contributions from both types of scattering: in the spectral region below 600 nm the character of scattering is predominantly described by the Mie theory, and above

600 nm – by the superposition of both theories. The validity of the last statement follows also from the analysis of the dependence of μ_s on the wavelength in the range 600–1000 nm, presented in the inset of Fig. 2a in logarithmic scale. This dependence cannot be approximated with good accuracy in the entire range mentioned above by a power function, which in logarithmic scale is plotted by a linear dependence. Therefore, the determination of the power of the function in the considered case can be performed only locally, in a narrow (not greater than 100 nm) interval of wavelengths. The estimates show that the slope coefficient of the analysed dependence monotonically changes from –0.6 in the vicinity of 600 nm to –2.6 in the vicinity of 1000 nm. This fact demonstrates that with a decrease in the ratio of the particle size and the wavelength, the contribution from the Rayleigh scattering, characterised by the power –4, becomes dominant.

The comparative analysis of the scattering efficiency (Fig. 2) shows that for the grinded PS particles the values of μ_s are at least by three times larger than those of the ablated nanoparticles if the volume concentration of the first ones is by three times smaller than that of the second ones. Therefore, it may be ascertained that the efficiency of light scattering in aqueous solutions of silicon nanoparticles formed by means of the electrochemical etching method with subsequent grinding, is greater by nearly an order of magnitude than in suspensions formed using pulsed laser ablation. There can be two reasons explaining such a great difference. The first reason is that the larger-size particles possess a larger coefficient μ_s (see Section 3.1). The second reason is related to the developed specific area of the PS that facilitates an increase in the number of scattering events and, therefore, the photon lifetime in the mesoscopic medium. For the studied PS layers this assumption is confirmed by the considerable value of their diffuse reflection (Fig. 3), which monotonically increases with increasing wavelength in the range 450–1050 nm and approaches 50% in the near-IR range. The mirror reflection coefficient in this case does not exceed a few percent.

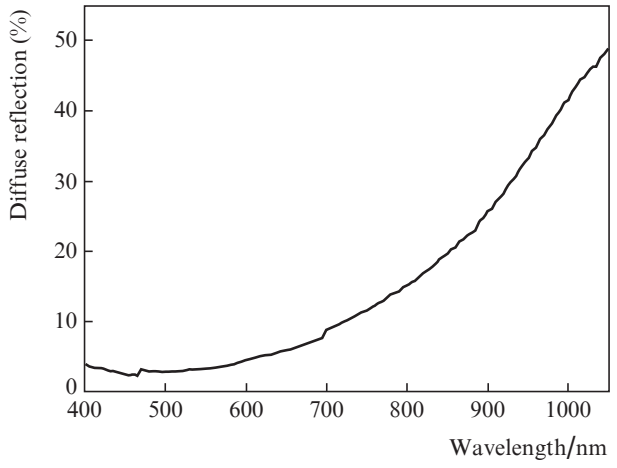

Figure 3. Diffuse reflection spectrum of the porous silicon film.

The significant diffuse reflection can be explained by the multiple scattering of light in the mesoscopic PS structure. The growth of the signal with the wavelength, as mentioned above, is related to a decrease in the light absorption by silicon in the red and near-IR spectral regions and is confirmed by a monotonic decrease in the coefficients μ_a in Fig. 2b for the studied PS powder.

3.2. Experimental study of the contrast effect of silicon nanoparticles in OCT

The high efficiency of radiation scattering in near-IR range by silicon nanoparticles, in particular, backscattering, in combination with low absorption and biocompatibility are the reasons for their high applicability for contrasting the OCT images of biotissues. In order to study the efficiency of the silicon nanoparticles used as contrast agents in OCT imaging, we compared experimentally both types of the studied nanoparticles, i. e., the ones obtained by laser ablation and by mechanical grinding of PS into a powder.

To compare the efficiency of using these two types of nanoparticles we obtained the OCT images of the agar gel surface used as a biotissue phantom. The surface was covered either with a suspension of nanoparticles produced using laser ablation (Fig. 4a), or with the PS powder (Fig. 4b). In the first case, a drop of the studied suspension was applied on the surface. The most part of the particles did not penetrate deep into the agar gel and settled at the interface, thus increasing its contrast. In the second case, the agar surface was directly covered with a layer of the PS powder and the contrast was

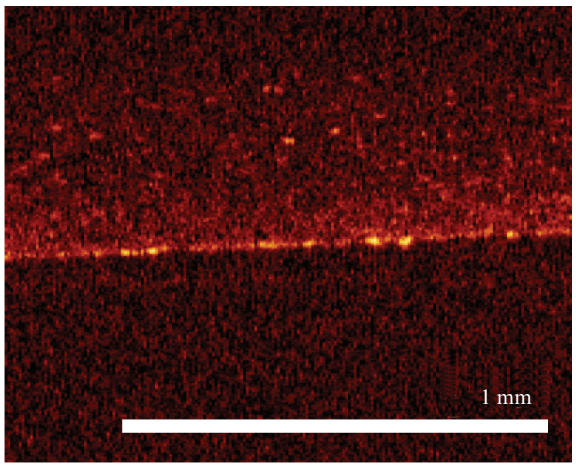

a

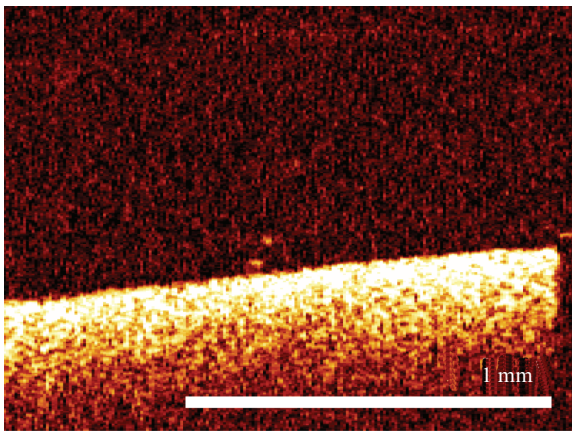

b

Figure 4. OCT images of the agar gel surface covered with the suspension of silicon nanoparticles prepared using (a) laser ablation in water and (b) porous silicon powder. The centre probe wavelength is 910 nm.

enhanced due to multiple scattering. It is worth noting that in the case of the suspension, even with the sedimentation taken into account, the concentration of the particles at the surface of the agar phantom was essentially lower than in the case of the powder. This fact gave rise to the essential difference in the signal level from the boundary when using the particles obtained by laser ablation and the powder of porous silicon (Figs 4a and 4b, respectively). Moreover, in the considered case, the environment for the particles obtained using laser ablation is water, and for the PS particles it is air, which leads to a considerable jump in the relative refractive index and, therefore, to more efficient scattering. Note that in the absence of particles, the signal from the phantom boundary was at the level of noise and did not exceed 5 dB. When using silicon nanoparticles, the maximal contrast of the boundary in the above-mentioned cases amounted to 14 and 30 dB for the particles obtained by laser ablation and for the PS powder, respectively, which characterises both types of particles as efficient contrast agents.

It is worth noting that the observed difference between the contrast in the phantom images, obtained with the particles of different types at comparable volume concentrations, agrees well with the results of spectrophotometry for the coefficient μ_s (Fig. 2), since the light scattering by PS is also much more efficient than for the ablated nanoparticles. This is due to their larger size and developed specific surface (see Section 3.1). On the other hand, the nanoparticles having a size above 100 nm are not always suitable for particular applications in the diagnostics of biological or mimicking tissues because of the difficulty of introducing them into the studied objects and the increased biodegradation time in comparison with the case of smaller particles.

Thus, in spite of the biocompatibility, demonstrated for a wide class of silicon nanoparticles, the studies of biological safety of the considered particles have not been carried out yet and, therefore, our studies were restricted to the phantom experiments.

3.3. Numerical simulation of the contrast effect of silicon nanoparticles in OCT imaging

Preliminary comparison of the estimates and TEM, SEM and DLS data has shown that the main contribution to the optical characteristics is made by the particles of large size, even though their concentration in the suspension is relatively small (about a few percent of the total number of particles).

The efficiency of silicon nanoparticles as contrast agents in real biotissues can be estimated before getting the information about their biocompatibility using the methods of numerical simulation. The Monte Carlo method is most efficient in the modelling of two- and three-dimensional OCT images, since it allows the consideration of complex geometry and optical inhomogeneity of biotissues.

Using the Mie theory, we estimated the optical properties of suspensions of nanoparticles having different diameters and volume concentration of 10^{13} cm^{-1}. In the above considerations, this concentration was shown to be characteristic for the studied nanosystems.

We should not forget that the present approach implies *a priori* that the scatterers are spherical. However, within the frameworks of the performed analysis of the optical properties of suspensions, when the stochastically oriented nonspherical scatterers are present (see Fig. 1e), this theory is also applicable for the estimation of scattering characteristics. In this case, μ_s and μ_a can be determined either as a single Mie solution for a sphere having the effective radius value, or as a series of Mie solutions with multiple radii.

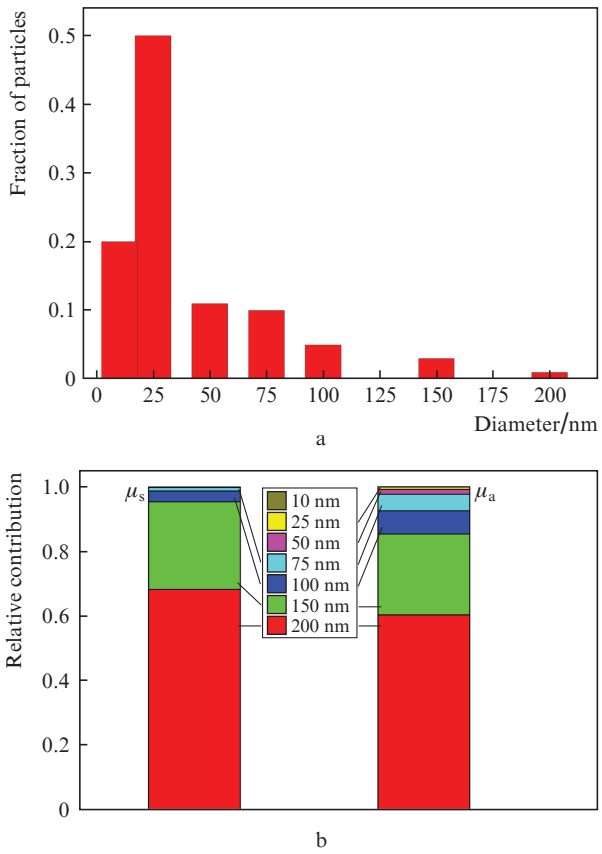

Figure 5. (Colour online) (a) Size distribution of silicon nanoparticles in the suspension used in the simulation and (b) relative contribution of the particles having different diameters to the values of the scattering and absorption coefficients of the suspension.

In the simulation, we used the size distribution of the particles presented in Fig. 5a and considered the suspension with a total concentration of 10^{13} cm^{-1}. This distribution provides the following optical properties of the suspension: μ_s = 7.78 mm^{-1}, μ_a = 0.05 mm^{-1}, g = 0.36, where g is the anisotropy factor (the mean cosine of the scattering angle). The relative contribution of the particles, having a different size, to the values of the optical properties is shown in Fig. 5b.

As a simulated biotissue, we used a multilayer model of human skin shown in Fig. 6. The optical properties of the layers, used in the simulation, were obtained by averaging the literature data and are summarised in Table 1. The model image (Fig. 7b) corresponds to the morphological structure of human skin and agrees with the experimental OCT image of

Table 1. Optical parameters of the skin layers.

Skin layer	μ_s /mm^{-1}	μ_a /mm^{-1}	g	n
Stratum corneum*				
Epidermis	5	0.015	0.95	1.37
Upper layers of reticular dermis	12	0.02	0.85	1.4
Deep layers of reticular dermis	12	0.1	0.9	1.39

Note. The stratum corneum is modelled by the surface roughness with the amplitude 4 μm; n is the refractive index.

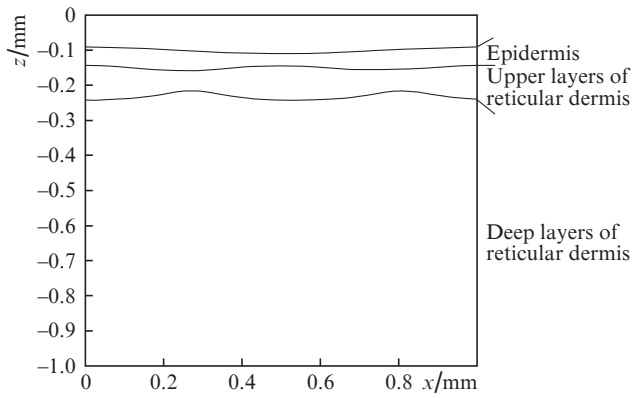

Figure 6. Multilayer model of skin used in the simulations.

the skin (Fig. 7a). The advantage of numerical simulation as compared to the real experiment consists in the possibility of modelling an OCT system with a more sensitive detector, which provides greater imaging depth.

In the modelling, we assumed that in the skin a spherical structural element is present having a radius of 50 μm, which does not differ from the surrounding biotissues in its optical properties, but is capable of accumulating nanoparticles in the concentration corresponding to that in the suspension. In this case, the absorption and scattering coefficients are added to their background values in the biotissue. The OCT images of skin were modelled for different depths of nanoparticles deposition (Fig. 8). The considered inhomogeneity can be the model image of a hair bulb, pore, or duct, capable of accumulating nanoparticles, introduced by surface application of injection.

At the considered deposition depths, the image of the spherical inhomogeneity is efficiently contrasted, the contrast decreasing with depth. At depths of 100–200 μm in the model OCT images the essential reduction of the OCT signal coming from under the contrasted region is observed, which is due to the significant attenuation of the probe beam due to inhomogeneity.

Thus, the results of numerical simulation have demonstrated that the considered particles used at the skin surface and at depths not exceeding 200 μm, corresponding to the epidermis and upper layers of reticular dermis (see Fig. 6) possess high potentiality as OCT contrast agents.

As mentioned above, the experimental determination of the concentration of nanoparticles penetrated into different structural layers of real biotissues was not carried out in the present paper. However, the visualisation of the agar gel phantom and the calculations performed by us show that the used concentration 10^{13} cm^{-1} of silicon nanoparticles is quite enough for efficient contrast at least of the biotissue surface. Moreover, if we assume the suspension to penetrate into the tissue pores in the unchanged form, then the above concentration and high contrast are also attainable.

4. Conclusions

We have performed a comparative analysis of two types of silicon nanoparticles: nanoparticles obtained by laser ablation in liquids and nanoparticles obtained by electrochemical etching with subsequent mechanical grinding. The studies performed by electron microscopy have shown that the first type of nanoparticles is characterised by two predominant fractions with the particle size 2–40 nm and 70–200 nm, while the second type consists of one fraction with the size of nanoparticles varying from 50 to 300 nm. The study of optical properties of these nanoparticles revealed the efficient scattering of visible and near-IR radiation, which make it possible to expect promising potentialities of using the particles as contrast agents in the OCT imaging, confirmed in the experiment with the biotissue phantom. The numerical modelling of the OCT images of a biotissue with complex structure, simulating human skin with the local presence of silicon nanoparticles also confirmed their efficiency as contrast agents. In this case it has been shown that the dominant contribution to the effect is made by the fraction of large (150–300 nm) particles.

Acknowledgements. The formation of the particles, the study of their physical properties and the experimental OCT studies

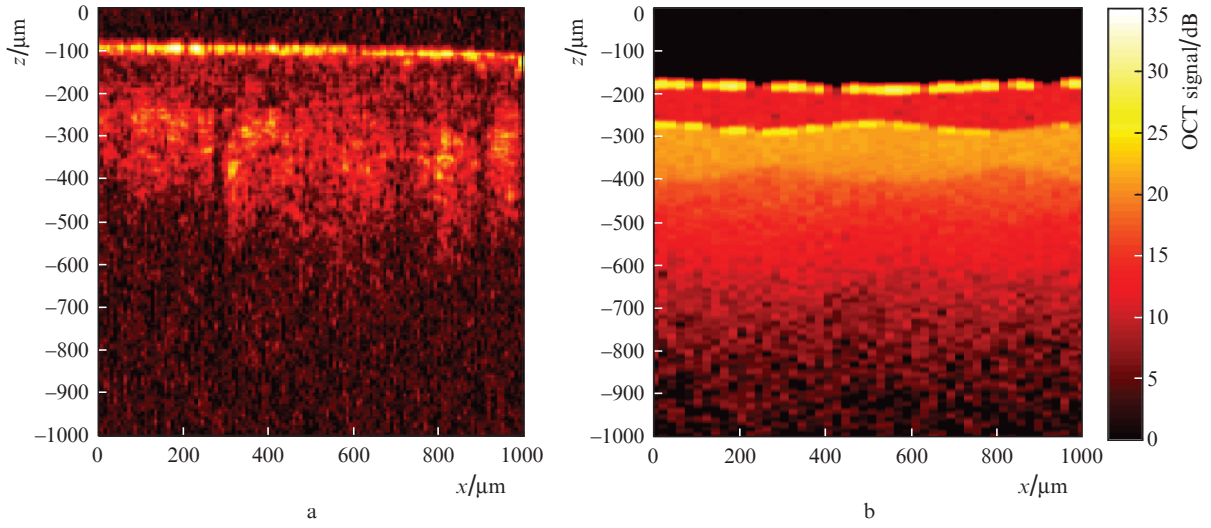

Figure 7. (a) Experimental and (b) model OCT images of human skin.

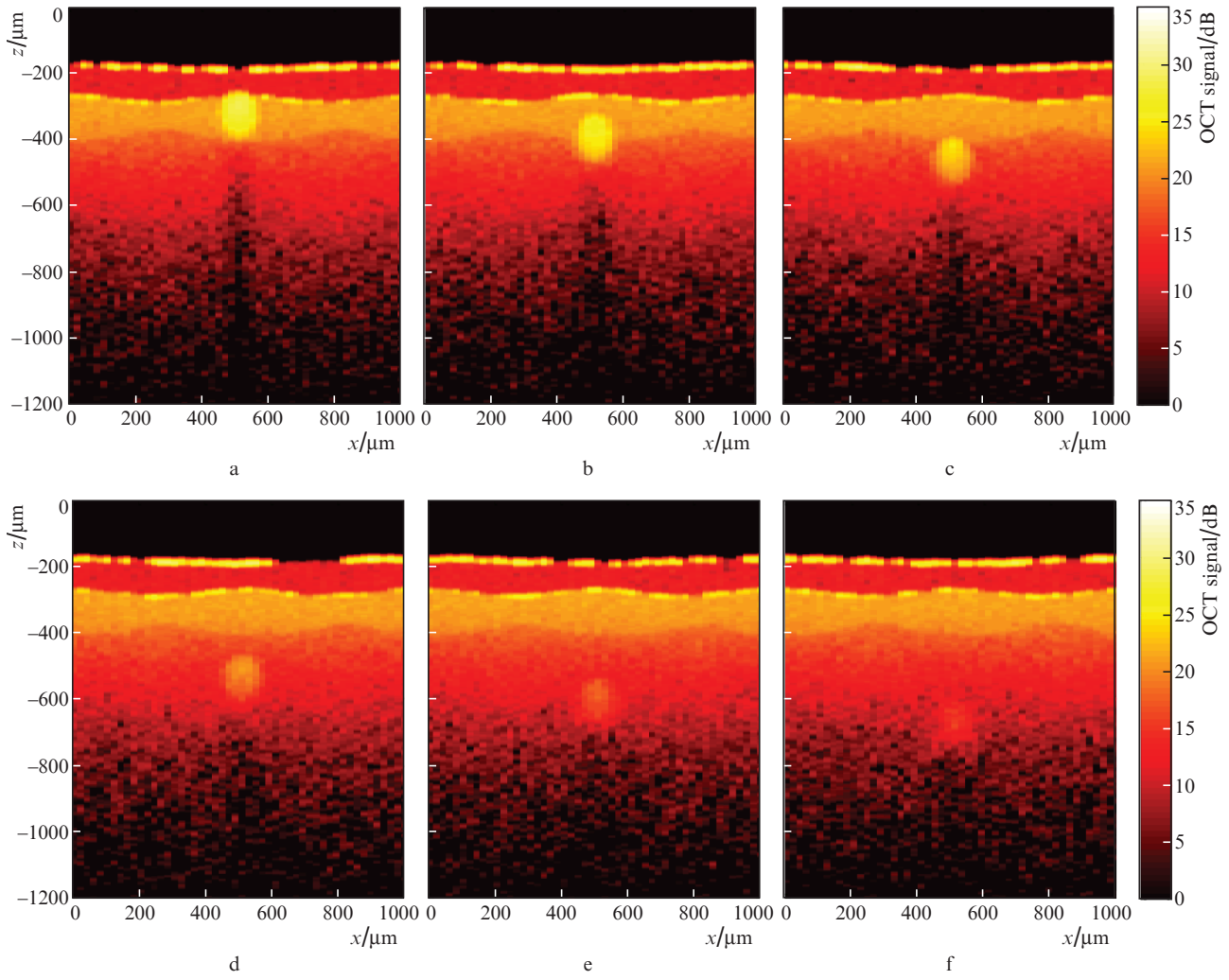

Figure 8. Model OCT images of human skin in the presence of s spherical inhomogeneity with the radius 50 μm, contrasted with the suspension of silicon nanoparticles with a concentration 10^{13} cm^{-3} for the depths of its deposition (a) 100, (b) 150, (c) 200, (d) 250, (e) 300 and (f) 350 μm.

were supported by the Russian Foundation for Basic Research (Grant No. 15-32-20227). The numerical simulation was supported the Ministry of Education and Science of the Russian Federation (Agreement No. 14.Z50.31.0022).

The authors are grateful to A.A. Ezhov, S.S. Abramchuk, and D.E. Presnov for help in obtaining TEM and SEM images of silicon nanoparticles.

References

1. Kim H.-Y., Lee K., Lee J.W., Kim S., Kim G.-T., Duesberg G.S. *J. Appl. Phys.*, **114** (14), 144503 (2013).
2. Li Y., Qian F., Xiang J., Lieber C.M. *Mat. Today*, **9** (10), 18 (2006).
3. Mamichev D.A., Gonchar K.A., Timoshenko V.Yu., Mussabek G.K., Nikulin V.E., Taurbaev T.I. *J. Raman Spectrosc.*, **42** (6), 1392 (2011).
4. Chen S., Xie Y., De A., van den Berg A., Carlen E.T. *Appl. Phys. Lett.*, **103** (17), 173702 (2013).
5. Zörgiebel F.M., Pregl S., Römhildt L., Opitz J., Mikolajick T., Baraban L., Cuniberti G. *Nano Res.*, **7** (2), 263 (2014).
6. Huang Y., Duan X., Lieber C.M. *Small*, **1** (1), 142 (2005).
7. Tian B., Zheng X., Kempa T.J., Fang Y., Yu N., Yu G., Huang J., Lieber C.M. *Nature*, **449** (7164), 885 (2007).
8. Emelyanov A.V., Khenkin M.V., Kazanskii A.G., Forsh P.A., Kashkarov P.K., Gecevicius M., Beresna M., Kazansky P.G. *Thin Solid Films*, **556**, 410 (2014).
9. Park J.-H., Gu L., von Maltzahn G., Ruoslahti E., Bhatia S.N., Sailor M.J. *Nature Mater.*, **8** (4), 331 (2009).
10. Gongalsky M.B., Kharin A.Yu., Osminkina L.A., Timoshenko V.Yu., Jeong J., Lee H., Chung B.H. *Nanoscale Res. Lett.*, **7**, 446 (2012).
11. Blandin P., Maximova K.A., Gongalsky M.B., Sanchez-Royo J.F., Chirvony V.S., Sentis M., Timoshenko V.Yu., Kabashin A.V. *J. Mater. Chem. B*, **1** (19), 2489 (2013).
12. Gongalsky M.B., Osminkina L.A., Pereira A., Manankov A.A., Fedorenko A.A., Vasiliev A.N., Solovyev V.V., Kudryavtsev A.A., Sentis M., Kabashin A.V., Timoshenko V.Yu. *Sci. Rep.*, **6**, 24732 (2016).
13. Ryabchikov Y.V., Belogorokhov I.A., Gongalskii M.B., Osminkina L.A., Timoshenko V.Yu. *Semiconductors*, **45** (8), 1059 (2011) [*Fiz. Tekh. Poluprovodn.*, **45** (8), 1090 (2011)].
14. Gongalsky M.B., Kharin A.Yu., Zagorodskih S.A., Osminkina L.A., Timoshenko V.Yu. *J. Appl. Phys.*, **110** (1), 013707 (2011).
15. Osminkina L.A., Gongalsky M.B., Motuzuk A.V., Timoshenko V.Yu., Kudryavtsev A.A. *Appl. Phys. B*, **105** (3), 665 (2011).
16. Osminkina L.A., Tamarov K.P., Sviridov A.P., Galkin R.A., Gongalsky M.B., Solovyev V.V., Kudryavtsev A.A., Timoshenko V.Yu. *J. Biophoton.*, **5** (7), 529 (2012).
17. Rioux D., Laferriere M., Douplik A., Shah D., Lilge L., Kabashin A.V., Meunier M.M. *J. Biomed. Opt.*, **142**, 021010 (2009).
18. Ksenofontova O.I., Vasin A.V., Egorov V.V., Kiselev O.I., Bobyl' A.V., Soldatenkov F.Yu., Terukov E.I., Ulin V.P., Ulin N.V. *Tech. Phys.*, **51** (1), 66 (2014) [*Zh. Tekh. Fiz.*, **84** (1), 67 (2014)].

19. Kilpeläinen M., Riikonen J., Vlasova M.A., Huotari A., Lehto V.P., Salonen J., Herzig K.H., Järvinen K. *J. Control. Release.*, **137**, 166 (2009).
20. Low S.P., Williams K.A., Canham L.T., Voelcker N.H. *Biomaterials*, **27**, 4538 (2006).
21. Laaksonen T., Santos H., Vihola H., Salonen J., Riikonen J., Heikkila T., Peltonen L., Kumar N., Murzin D.Yu., Lehto V.-P., Hirvonen J. *J. Chem. Res. Toxicol.*, **20**, 1913 (2007).
22. Chiappini C., Liu X., Fakhoury J.R., Ferrari M. *Adv. Funct. Mater.*, **20**, 2231 (2010).
23. Gu L., Ruff L.E., Qin Z., Corr M., Hedrick S.M., Sailor M.J. *Adv. Mater.*, **24**, 3981 (2012).
24. Besner S., Kabashin A.V., Winnik F.M., Meuiner M. *Appl. Phys. A*, **93**, 955 (2008).
25. Correard F., Maximova K., Estève M.-A., Villard C., Roy M., Al-Kattan A., Sentis M., Gingras M., Kabashin A.V., Braguer D. *Int. J. Nanomed.*, **9**, 5415 (2014).
26. Omelchenko A.I., Sobol E.N., Simakin A.V., Serkov A.A., Sukhov I.A., Shafeev G.A. *Laser Phys.*, **25**, 025607 (2015).
27. Soshnikova Yu., Omelchenko A., Shekhter A., Sobol E. *Magnetite Nanoparticles for Diagnostics and Laser Repair of Cartilage in Nanobiomaterials in Hard Tissue Engineering. Applications of Nanobiomaterials* (Amsterdam: Elsevier, 2016) Vol. 4.
28. Soshnikova Yu.M., Roman S.G., Chebotareva N.A., Baum O.I., Obrezkova M.V., Gillis R.B., Harding S.E., Sobol E.N., Lunin V.V. *J. Nanopart. Res*, **15**, 2092 (2013).
29. Eroshova O.I., Zabotnov S.V., Gongal'skii M.B., Ezhov A.A., Golovan' L.A., Kashkarov P.K., Perminov P.A. *Crystallogr. Rep.*, **57** (6), 831 (2012) [*Kristallografiya*, **57** (6), 942 (2012)].
30. Kuzmin P.G., Shafeev G.A., Bukin V.V., Garnov S.V., Farcau C., Carles R., Warot-Fontrose B., Guieu V., Viau G. *J. Phis. Chem.*, **114**, 15266 (2010).
31. Kusi-Appiah A.E., Mastronardi M.L., Qian C., Chen K.K., Ghazanfari L., Prommapan P., Kübel C., Ozin G.A., Lenhert S. *Sci. Rep.*, **7**, 43731 (2017).
32. Shiohara A., Prabakar S., Faramus A., Hsu C.-Y., Lai P.-S., Northcotea P.T., Tilley R.D. *Nanoscale*, **3**, 3364 (2011).
33. Philipp H.R., Taft E.A. *Phys. Rev.*, **120** (1), 37 (1960).
34. Kirillin M.Yu., Shirmanova M.V., Sirotkina M.A., Bugrova M.L., Khlebtsov B.N., Zagaynova E.V. *J. Biomed. Opt.*, **14**, 021017 (2009).
35. Khlebtsov N.G. *Quantum Electron.*, **38** (6), 504 (2008) [*Kvantovaya Elektron.*, **38** (6), 504 (2008)].
36. Popov A.P., Zvyagin A.V., Lademann J., Roberts M.S., Sanchez W., Priezzhev A.V., Myllylä R. *J. Biomed. Nanotech.*, **6** (5), 432 (2010).
37. John S., Marpu S., Li J., Omary M., Hu Z., Fujita Y., Neogi A. *J. Nanosci. Nanotechnol.*, **10** (3), 1707 (2010).
38. Kirillin M.Yu., Sergeeva E.A., Agrba P.D., Krainov A.D., Ezhov A.A., Shuleiko D.V., Kashkarov P.K., Zabotnov S.V. *Laser Phys.*, **25** (7), 075604 (2015).
39. Tearney B., Bouma B. (eds.) *Handbook of Optical Coherence Tomography* (Boca Raton: CRC Press, 2001).
40. Perminov P.A., Dzhun I.O., Ezhov A.A., Zabotnov S.V., Golovan L.A., Ivlev G.D., Gatskevich E.I., Malevich V.L., Kashkarov P.K. *Laser Phys.*, **21** (4), 801 (2011).
41. Kirillin M., Meglinski I., Kuzmin V., Sergeeva E., Myllylä R. *Opt. Express*, **18** (21), 21714 (2010).
42. Bohren C.F., Huffmann D.R. *Absorption and Scattering of Light by Small Particles* (New York: Wiley-Interscience, 2010).
43. Petrov Yu.I. *Klastery i malye chastitsy* (Clusters and Small Particles) (Moscow: Nauka, 1986).
44. Wood R.F., Leboeuf J.N., Geohegan D.B., Puretzky A.A., Chen K.R. *Phys. Rev. B*, **58** (3), 1533 (1998).
45. Alekhin A.I., Perminov P.A., Kashkarov P.K., Zabotnov S.V., Golovan' L.A. *J. Opt. Technol.*, **78** (3), 161 (2011) [Alekhin A.I., Perminov P.A., Zabotnov S.V., Golovan L.A., Kashkarov P.K. *Opt. Zh.*, **78** (3), 10 (2011)].
46. Rouquerol J., Avnir D., Fairbridge C.W., Everett D.H., Haynes J.H., Pernicone N., Ramsay J.D.F., Sing K.S.W., Unger K.K. *Pure Appl. Chem.*, **66**, 1739 (1994).
47. Matveev A.N. *Optika* (Optics) (Moscow: Vysshaya shkola, 1985).
48. Loginova D.A., Krainov A.D., Agrba P.D., Sergeeva E.A., Kirillin M.Yu. *Quantum Electron.*, **46** (6), 528 (2016) [*Kvantovaya Elektron.*, **46** (6), 528 (2016)].